Three-dimensional, Time-resolved (4D) Relative Pressure Mapping using Magnetic Resonance Imaging

Authors:

J. Michael Tyszka, Ph.D.

† David H. Laidlaw, Ph.D.,

* Joseph W. Asa, B.S.

Jeffrey M. Silverman, M.D.

Department of Imaging, Cedars-Sinai Medical Center

8700 Beverly Blvd., Los Angeles CA 90048

† Division of Biology, California Institute of Technology, Pasadena, CA and Computer Science Department, Brown University, Providence RI

* The Observatories, Carnegie Institution of Washington, Pasadena, CA

Running Title: 4D Pressure Mapping

Corresponding author and reprints:

J. Michael Tyszka, Ph.D.

Division of Surgery, L002B

City of Hope National Medical Center

1500 E. Duarte Rd., Duarte CA 91010

Tel: (626) 359-8111 x 5633

Fax: (626) 301-8855

Email: jmt@gg.caltech.edu

ABSTRACT

We describe here a method for generating relative pressure maps from magnetic resonance velocity data in three spatial and one temporal dimension (4D). The relative pressure map calculated for pulsatile flow in a compliant phantom was shown to be consistent with independent pressure transducer measurements. The feasibility of performing 4D pressure mapping *in vivo* is also demonstrated.

Key Words

Magnetic resonance imaging

Blood pressure measurement

Phase-constrast velocity measurement

Four-dimensional imaging

INTRODUCTION

Magnetic resonance imaging (MRI) allows true three-dimensional, time-resolved (4D) measurements of velocity with negligible risk to the subject. It has been shown that relative pressure may be calculated numerically from velocity data using fluid dynamics relations, but so far this calculation has been limited to two-dimensional, time-resolved MRI data (1-3). Extension to 4D imaging is a natural progression from the existing methods and is more appropriate for the solution of the Navier-Stokes equations within complex vessel geometries. A robust and non-invasive method for calculating 4D pressure maps within the human cardiovascular system has the potential to impact both the understanding and clinical management of cardiovascular disease.

Blood pressure is a fundamental physiological parameter in many areas of medicine. Blood pressure measurements are most commonly made using a cuff manometer that gives a generalized estimate of absolute systolic and diastolic pressure at one spatial point in the peripheral cardiovascular system (4). Introduction of a pressure catheter into the central cardiovascular system allows at best a one-dimensional spatially resolved pressure measurement but with greatly increased temporal resolution throughout the cardiac cycle. Although cardiac catheterization is considered to be a low risk procedure, it is far from non-invasive (5,6).

Calculation of pressure gradients and relative pressure from time-resolved velocity measurements has been studied extensively (1,3,7-13). The pressure gradient across a vessel stenosis or restricted valve orifice is commonly estimated using a simplified form of the Bernoulli equation and measurements of the peak velocity in the distal flow jet. Despite the fact that this estimate depends on many broad assumptions about the nature of flow in a stenosis, it has been shown to have clinical value (7,9). However, such point estimates provide no information about the temporal or spatial variation of pressure around the stenosis and would not apply to more generalized flow regimes.

Recently, velocity data acquired using time-resolved MRI have been used to estimate relative pressure using more sophisticated theory. The most popular method for acquiring velocity information using MRI is phase-contrast (PC) imaging (14,15). Although 2D time-resolved (2D CINE) PC studies are common, the acquisition of 4D PC images is rarely reported due to the extended imaging times required (16). However,

recent advances in gradient hardware have significantly reduced the imaging time for 4D PC data to the point where sufficient data for 4D pressure mapping can be generated in less than 15 minutes.

Two approaches to relative pressure calculation from CINE PC data have emerged, both based on the Navier-Stokes equation relating a three-dimensional velocity vector field to the pressure gradient vector field for an incompressible fluid. The Navier-Stokes equation describes the time-varying flow of a viscous, incompressible fluid and can be expressed as:

$$-\nabla p = \rho\left(\frac{\partial \mathbf{v}}{\partial t} + (\mathbf{v}.\nabla)\mathbf{v} - \mathbf{g}\right) - \mu\nabla^2\mathbf{v} \qquad (1)$$

where p is pressure, $\mathbf{v}$ is velocity, ρ is fluid density, $\mathbf{g}$ is the gravitational body-force and μ is the fluid viscosity. This equation is normally coupled with the divergence-free condition due to the incompressibility of the fluid:

$$\nabla \cdot \mathbf{v} = 0 \qquad (2)$$

The first Navier-Stokes method, studied extensively by Urchuk *et al.* (1,2,10,11), was originally developed for estimating aortic wall compliance and pulse wave velocity. Simplification of the Navier-Stokes equation leads to a wave equation relating the second-order temporal and spatial derivatives of the mean velocity. The vascular wall compliance can then be estimated by correlating the second-order derivatives calculated from mean velocity sampled throughout the cardiac cycle. In this case, compliance was defined as:

$$C = \frac{1}{A}\frac{\partial A}{\partial P} \qquad (3)$$

where A is the instantaneous cross-sectional area of the tube at a given point, and P is the pressure within the tube relative to the pressure outside the tube. The compliance was calculated from the linear correlation coefficient between the spatial and temporal second-order derivatives of the spatial mean of the velocity component ($\overline{V}_z$) parallel to the long axis (z) of the tube.

A partial differential equation (PDE) for the mean intra-vascular pressure was derived assuming that the pressure-induced changes in aortic cross-sectional areas are small:

$$\frac{\partial p}{\partial t} \approx -\frac{1}{C}\frac{\partial \bar{v}_z}{\partial z} \tag{4}$$

However, the temporal variation of the absolute pressure cannot be determined since the integration constant for the differential equation is unknown. The method was also limited to the aorta where the time-varying cross-sectional area and therefore the wall compliance could be accurately determined using MR imaging. This method does not generate a map of pressure but allows a spatial average to be determined at several points along the artery's length. The implementation described by Urchuk *et al.* was based on 2D multi-slice MRI and not a true 3D acquisition and would not perform well in smaller, curving vessels due to the large (10mm) slice thickness employed. This approach was shown to yield results with a RMS error between 4% and 12% (1,10).

A second approach to MR pressure mapping uses the Navier-Stokes equation to calculate the relative pressure at every point in a 2D CINE MRI velocity map (3). The pressure gradient vector at every point within a vessel can be calculated directly from the velocity vector and its derivatives using Eq.(1). Relative pressure can then be calculated from the pressure gradient by iterative refinement of the integration. Finite sampling, the point-spread function, noise, and image artifacts each introduce errors into the pressure gradient image and, in turn, into the pressure image. This approach, while generating a map of relative pressure, was limited in many ways, by both the data acquisition method and the pressure calculation algorithm. A 2D phase-contrast magnetic resonance pulse sequence was used to acquire *in vivo* data. The calculation of pressure from the pressure gradient required that boundary conditions be applied to the flow at the walls of the vessel. In order to determine the boundary position, a manual segmentation was performed using the magnetization magnitude images without partial volume treatment. Some of the phenomena not included in this pressure calculation algorithm were discussed, including partial volume effects and phase errors due to high orders of motion. For the *in vivo* relative pressure calculation, only the in-plane components of velocity were used and viscosity was ignored. Limitations on the total imaging time precluded the acquisition of a 3D dataset.

We present here a method for deriving 3D time-resolved relative pressure maps from 4D PC images of flow within compliant walled tubing or vessels. The results of the numerical method used to calculate

pressure from velocity are compared to independent pressure transducer measurements made in a compliant-walled flow phantom. The same method is also demonstrated in a normal human subject and used to calculate the 4D relative pressure map within the thoracic aorta.

MATERIALS AND METHODS

All imaging studies were performed using a 1.5 Tesla Horizon EchoSpeed imager (General Electric Medical Systems, Milwaukee, WI) capable of a maximum gradient strength of 22mT/m with a slew rate of 120T/m/s. 4D PC velocity imaging (16) was implemented using a custom-written pulse sequence. The imaging sequence was found to be capable of a minimum TR/TE of 10.5ms/3.5ms for a maximum velocity encoding (VENC) of 1600mm/s and 11.5ms/4.2ms for a VENC of 300mm/s. All three components of velocity were encoded using an unbalanced four-point phase-difference approach (17). A segmented k-space trajectory was used to reduce total acquisition time at the expense of temporal resolution (16). The phase of the cardiac cycle was estimated by the system gating hardware in real-time and recorded separately from the image data by the pulse sequence software. This allowed a more accurate and truly retrospective re-calculation of the cardiac phase corresponding to a particular data acquisition. Cardiac phases were recorded for every group of four velocity encodings.

All 4D PC data were transferred to a UNIX graphics workstation cluster for reconstruction. The cardiac phase for each velocity encoding group was recalculated retrospectively and used to generate temporal phases via a nearest-neighbor approach to k-space filling. The number of phases was chosen to avoid temporal aliasing using the methods of Polzin *et al.* (18). All components of flow were phase baseline corrected using four regions of presumed stationary material as references. This baseline correction was in response to variations in the measured phase across the imaging volume caused by gradient eddy currents. The median phase in each location was calculated over a 3x3x3 voxel kernel and the trilinear phase baseline was derived and subtracted from each component. Regions of aliased velocity in the phantom data due to inflow jetting at the entrance to the latex tube were unwrapped using a conventional region-growing algorithm (19).

Pressure calculation was restricted to a single contiguous volume within each dataset by a simple segmentation approach. The volume of interest was defined by filling from a seed point while using

threshold constraints on both flow speed and magnetization magnitude. The resulting mask data consisted of voxels with zero value outside the filled region and one inside the filled region representing flowing material. This volume data was then blurred using a 1.0 pixel radius Gaussian filter to generate a naïve inside-outside (I/O) function. An I/O function represents the position of a pixel relative to a boundary and varies smoothly with distance from the boundary. In this study, the boundary was either the interface between flowing fluid and air in the phantom, or the aortic wall *in vivo*. The I/O function used in this study varied from 0.0 fully outside the segmented volume to 1.0 fully inside, passing smoothly through 0.5 at the approximate location of the boundary. The I/O function representation of a region allows dilation or erosion of a boundary simply by altering an acceptance threshold, and also allows crude estimation of distance from a boundary to a given voxel. Both these features were used in the subsequent pressure calculation.

The relative pressure field was calculated independently for each time-step using a method similar to that proposed by Yang *et al.* (3). The pressure gradient was calculated first using Eq.(1) at all points within the imaging volume. This included some voxels within the moving fluid contaminated by partial volume effects at vessel boundaries and voxels in stationary tissue and air. The pressure gradient data was median filtered using a 3x3x3 kernel to reduce noise at the expense spatial resolution. All velocity derivatives were calculated using discrete central-differences. Relative pressure was determined iteratively within the volume defined by I/O function values greater than 0.9. This restricted the pressure calculation to voxels within the moving fluid that were not significantly contaminated by stationary tissue. The iterative refinement of the pressure map was performed in a slightly different fashion from that used by Yang *et al.* (3). For each iteration, the pressure difference that would be expected at a given voxel based on the local pressure gradients to the six orthogonal neighbors was calculated. The pressure at this voxel was then replaced by a weighted sum of the current pressure and the mean of the six possible pressures calculated from the neighboring voxels:

$$p^{k+1} = (1-\alpha)\, p^{k} + \frac{1}{6}\alpha\left(\sum_{i}\left(p_i^{k} + \nabla p_i \cdot \Delta r_i\right)\right) \qquad (4)$$

where p^k is the pressure at the k^{th} iteration, i indicates one of the six orthogonal neighbors, ∇p_i is the pressure gradient at the i^{th} neighbor and Δr_i is the vector displacement from the current voxel to the i^{th}

neighbor. The value of α was set to 0.5 for all calculations. This recurrence relation was repeated until convergence, determined by a relative change in the mean pressure across the volume of less than 0.1%. The Navier-Stokes equation was assumed to be consistent within this volume and no boundary conditions on pressure at the vessel walls were used. The initial pressure estimate was generated by summation of the pressure gradient during flood-filling from a reference point in the descending aorta. The pressure at the reference point was defined as zero.

The divergence-free condition was not enforced explicitly under the assumption that the images represent an actual fluid and therefore the flow should naturally obey this condition.

A flow phantom was constructed which simulated the compliant characteristics of the normal human aorta. A 16cm length of latex rubber tubing with a diameter of approximately 25mm and a wall thickness of less than 1mm was attached between two transition sections which in turn coupled to PVC tubing leading out of the magnet room to the pump equipment (Figure 1). A domestic centrifugal pump placed in the fluid reservoir generated flow through the phantom. A DC-motor was used to rotate a ball valve placed downstream of the pump at a constant rate. Two flow modulating pulses were thus generated for every rotation of the faucet. Modulation frequencies of approximately 1.1Hz (68bpm) were obtained with a mean volume flow rate of 24.6 ml/s measured by timed volume collection over approximately 32 pulsatile cycles. The flow modulator was connected to the phantom in the bore of the magnet by lengths of PVC tubing approximately 20 feet in length. The flow waveform generated by the pump was very stable, period-to-period, and no attempt was made to modify its shape to mimic a physiological pattern.

A gating signal was generated using an optical switch monitoring the DC-motor drive shaft. Approximately 15ml of Magnevist (0.5M gadopentetate dimeglumine, Berlex Laboratories Inc., Wayne NJ) were added to 10.5 liters of tap water in the fluid reservoir (approximate concentration 0.75mM). This reduced the T_1 of the flowing water to the order of 250ms and helped increase the SNR of all phantom images. The gage pressure (pressure relative to atmospheric pressure) was measured using two piezo-resistive transducers (Honeywell Inc., Minneapolis MN) attached to the plastic transition sections at either end of the latex tube. The transducers were calibrated within the 1.5 Tesla field at the center of the magnet bore by varying the pressure head of water at the exit tube outside the magnet room with the flow modulator valve closed and the pump off. The output from both transducers and the gating signal were

digitized using a multi-channel analog-to-digital converter (Pico Technology Ltd., Cambridge, England) and recorded by a laptop computer.

Pressure waveforms from both transducers and the gating signal were acquired simultaneously for 64 seconds at a rate of 16ms/sample with both the modulator and pump running. MR images were not acquired simultaneously with transducer pressure experiments to avoid interference between the two modalities. Pressure waveform data were passed to a UNIX workstation and processed using custom-written software. The calibrated mean pressure waveform over the 64s sampling period from each transducer was calculated by Fourier interpolation of all waveforms to 128 points per cycle. The pressure difference between the two transducers was then calculated by simple subtraction of the two gage waveforms. The compliance of the latex tube wall was measured using cross-sectional images acquired over a range of calibrated pressures to confirm that it approximated the compliance of the thoracic aortic in normal adult humans.

All MR imaging of the phantom was performed using a general-purpose flexible linear receiver coil (General Electric Medical Systems, Milwaukee WI) which was wrapped around the entire central section of the phantom, containing the latex tube, pressure transducers and stationary fluid reference vials.

The time-varying velocity and volume flow rates within the latex tube were measured with the pump and flow modulator running. 4D PC images were acquired of the whole latex tube segment with the following imaging parameters: Maximum velocity encoding = 300mm/s, FOV = 240mm x 180mm x 48mm, voxel size = 1.9mm x 1.9mm x 3mm, TR/TE = 11.5/4.2ms, flip angle = 10°, 2 views/segment, 1 average. The flow encoding duration was 46ms, which allowed reconstruction of 19 unaliased temporal phases over a median pulsatile period of 880ms.

2D PC CINE images at the entrance, middle and exit of the latex tube were also acquired using the General Electric Medical Systems pulse sequence supplied with the MRI system to act as a reference for evaluation of the new 4D PC sequence data. The flow in the latex tube was essentially unidirectional so only one flow direction was encoded. The number of reconstructed temporal phases was chosen to avoid aliasing, using the methods of Polzin *et al.* (18). The longitudinal velocity component measured using this sequence was assumed to be more accurate than the 3D PC CINE by virtue of the higher temporal resolution and in-plane spatial resolution of the 2D sequence. The 2D PC CINE flow data were used only to

characterize inaccuracies in the 3D PC CINE velocity data and not to calculate pressure maps within the phantom. Imaging parameters for the 2D sequence were as follows: Maximum velocity encoding = 200mm/s, FOV = 200mm x 200mm, voxel size = 0.8mm x 0.8mm x 5mm, TR/TE = 18ms/, flip angle = 10 degrees, 1 average. The duration of one set of unidirectional flow encoded acquisitions was 36ms, allowing the reconstruction of 24 unaliased temporal phases with a mean cardiac period of 860ms.

A 4D PC velocity dataset was also acquired in a normal human subject. Informed consent was obtained according to an IRB approved protocol prior to imaging. 4D PC images were acquired with flow encoding in all three spatial directions. The imaging parameters were as follows: Velocity encoding = 1600mm/s, FOV = 320 x 240 x 48mm, voxel size = 2.5 x 2.5 x 3mm, TR/TE = 10.5/3.5ms, flip angle = 10°, 2 views/segment, 1 average, total imaging time 12 minutes 54 seconds. The duration of one complete set of flow encoded acquisitions was 42ms which allowed reconstruction of 20 unaliased cardiac phases for a median cardiac period of 840ms. Cardiac synchronization was achieved using a plethysmograph which was found to give a much more reliable trigger than conventional ECG leads in the presence of the high slew-rate gradient waveforms typical of the 4D PC sequence. The *in vivo* MR data therefore acquired a negative cardiac phase-shift relative to an ECG-triggered reconstruction. Image reconstruction was identical to that used for the phantom data.

Raw data was again transferred to the UNIX cluster for reconstruction as described above. An I/O function was generated from the magnitude-weighted flow speed image at peak systole only and used for all phases. Apart from this, the reconstruction and pressure calculation were identical to that used for the phantom data.

RESULTS

The compliance of the latex tubing increased with cross-sectional area and varied from approximately 3.8 %/kPa to 9.8 %/kPa (0.5%/mmHg to 1.3%/mmHg) over the range of applied pressures used to calibrate the transducers (Figure 3). It was noted that the compliance of the latex tube increased with distension. This is comparable to the compliance of the thoracic aorta in a normal, healthy human subject which has been measured at approximately 1%/mmHg (1).

A comparison of the longitudinal velocity and volume flow rate data acquired using a 2D PC CINE sequence with that acquired using the new 3D PC CINE shows good agreement between the two methods (Figure 2). The negative sign of the velocity and volume flow rate (VFR) measurements is a consequence of the flow encoding gradient direction, which was antiparallel to the primary flow direction in the tube in both sequences. The absolute temporal mean volume flow rate (VFR) in this experiment was 24.6ml/s by timed fluid collection (Figures 2d-2f). This compares well with the 2D results (|VRF| = 27.1ml/s, 25.9ml/s and 21.9ml/s in the entrance, middle and exit slices, respectively) but reveals the poorer accuracy of the 3D results (|VFR| = 25.5ml/s, 29.4ml/s and 33.2ml/s respectively).

The pressure difference between points at the center of the tube adjacent to the pressure transducers calculated from the 3D MR velocity images (Figure 4) compared very well with that measured by the pressure transducers (Figure 5). A linear correlation coefficient was calculated by cubic interpolation of the transducer pressure difference waveform to match the 19 sample times of the MRI data. The correlation coefficient, R, was 0.862 (n = 19, p = 0.000002, F-ratio test, Statistica for Windows, Statsoft Inc., Tulsa OK), reflecting a highly significant correlation between the two waveforms. The regression slope was 1.11, as opposed to an ideal 1.0, which is most likely a consequence of the frequency response of the 3D PC CINE sequence that attenuates higher-frequency components of the pressure waveform.

Relative pressure maps of the aorta in a normal human volunteer (Figure 6) reveal the expected pattern of pressure changes close to systole with little significant spatial or temporal pressure variation in diastole. The 4D pressure map was calculated relative to a reference point (point 0 in Figure 7) in the descending aorta where pressure was defined as zero in all cardiac phases. The accelerative phase in early systole in marked by high pressure in the ascending aorta relative to the distal descending aorta in the 16^{th} through 18^{th} phases (600ms to 700ms after the plethysmograph trigger). During the decelerative phase following peak systole, the pressure distribution reverses in the 19^{th} through 20^{th} and 1^{st} through 4^{th} phases (700ms to 1000ms after the trigger, crossing into the next cardiac cycle). The reduced SNR of the *in vivo* dataset and the presence of a non-zero convective term both contributed to a noisier pressure gradient map, further underlining the importance of noise reduction, in this case by median filtering, prior to pressure integration. The relative pressure waveforms in the proximal descending aorta (Point A) and in the aortic arch (Point B) were extracted from this data (Figure 7). We see the early systolic accelerative phase as a positive deviation

in the relative pressure at both locations, with the pulse amplitude much greater in the aortic arch. The relative pressure then becomes negative at peak systole. There is a transient increase in relative pressure at approximately 800ms after the plethysmograph trigger, possibly due to the reflected pressure wave from the distal vasculature. A negative relative pressure at both locations represents the decelerative phase of aortic flow. The subjects' blood pressure was measured using an automatic cuff manometer and was found to be 120/77mmHg immediately prior to imaging and 114/73mmHg immediately following imaging, giving a mean pulse pressure of 42mmHg. The relative pressure pulse amplitude at the aortic arch was approximately 2.2kPa (16mmHg) from the MRI pressure map (Figure 7). This latter pulse amplitude is an underestimate of the true pressure pulse amplitude since the absolute pressure at the reference point also varies throughout the cardiac cycle. The relative pulse pressure of 16mmHg is the difference in pulse pressure between the aortic arch and the reference point.

DISCUSSION

We have demonstrated the feasibility of acquiring 4D PC data within a clinically acceptable time frame of less than 15 minutes, and the calculation of 4D relative pressure maps from such data. The use of 4D MR data has several advantages over multi-slice 2D CINE data for pressure calculation. The primary advantage is the reduction in voxel size in the third direction and the increase in SNR over a 2D sequence with identical voxel size. Approximately isotropic voxel dimensions across a volume reduce the need for geometric simplification or accurate imaging slice placement for the solution of the Navier-Stokes equation in three-dimensions.

The discrepancies between the 2D CINE and 4D results in the phantom cannot be assigned to partial volume errors alone, since the velocity at the tube center exhibits a similar error trend. The most likely cause of the VFR overestimation is residual eddy current effects untouched by the trilinear baseline correction algorithm. The greater gradient demands of the rapid 4D sequence are likely to increase eddy currents in the vicinity of the flow encoding pulses, which in turn affects the theoretical flow encoding moment at the echo. This error mechanism can be partially compensated during post-processing but ideally should be addressed at the data acquisition stage; the most recent developments in gradient hardware design may alleviate this problem. We expect the attenuation of the higher temporal frequency components of

flow to be more pronounced for the 4D sequence than for the 2D CINE sequnce, which accounts in part for the lower central velocity measured at the entrance to the latex tube (Figure 2a) where the pusatility is highest. The temporal bandwidth of the pressure waveform is limited by the bandwidth of the MR velocity data. According to Polzin *et al.* (18), the temporal frequency response of segmented PC CINE methods is a function of the time required to encode all velocity components and the number of views per segment. In this case the sample time was 46ms leading to a detectable bandwidth of ±21.7Hz. Two views per segment causes a greater attenuation of higher frequency pulsatile flow components than would be seen with only one view per segment, but does not affect the detectable bandwidth. A slight phase shift between the calculated pressure waveform and the transducer waveform is most probably due to a delay introduced by the trigger detection method of the gating system of the MR imager. The convective term of the Navier-Stokes equation is small throughout the phantom data since the tube was relatively straight. This term therefore contributes only a noise component to the calculated pressure gradient.

The *in vivo* pressure maps generated by this method cannot be directly compared to absolute pressure measurements made for example with a pressure catheter, since the reference point in the descending aorta is zeroed for all phases. Similarly, comparison of these results with cuff manometer readings is limited by the volume imaged, which does not include the brachial artery.

Although the divergence-free condition for incompressible fluids was assumed to be intrinsic to images of a real fluid, the use of finite sized imaging voxels and the presence of imaging noise both break this condition. We attempted to minimize gross errors due to incorporation of stationary tissue in voxels close to the vessel boundaries by restricting the calculation volume, but errors arising from partial volume effects within the moving fluid itself are still present. Image noise contains a divergent component that also breaks the divergence-free condition. Although a full analysis of the effect of partial volume effects and noise on the accuracy of the pressure calculation is beyond the scope of this study, ultimately these two sources of error should be addressed in future refinement of the pressure calculation algorithm.

We have demonstrated the feasibility of acquiring sufficiently high quality 4D PC data for pressure mapping in the aorta of a normal volunteer. Future validation of this technique should include direct correlation with invasive pressure measurements, either in an animal model, or in patients undergoing routine cardiac catheterization.

ACKNOWLEDGEMENTS

The authors wish to thank Miho Tyszka for assistance with data acquisition, Seth Blumberg for help coding parts of the pressure algorithm and Al Barr for use of the Caltech graphics laboratory. This work was supported in part by grants from Apple, DEC, Hewlett Packard, and IBM. Additional support was provided by NSF (ASC-89-20219) as part of the NSF STC for Computer Graphics and Scientific Visualization, by the DOE (DE-FG03-92ER25134) as part of the Center for Research in Computational Biology, and by the National Institute on Drug Abuse, the National Institute of Mental Health, and the National Science Foundation as part of the Human Brain Project.

REFERENCES

1. Urchuk SN, Plewes DB. MR measurement of time-dependent blood pressure variations. J Magn Reson Imaging 1995;5:621-7.

2. Urchuk SN, Fremes SE, Plewes DB. In vivo validation of MR pulse pressure measurement in an aortic flow model: preliminary results. Magn Reson Med 1997;38:215-23.

3. Yang GZ, Kilner PJ, Wood NB, Underwood SR, Firmin DN. Computation of flow pressure fields from magnetic resonance velocity mapping. Magn Reson Med 1996;36:520-6.

4. Harrison TR. Hypotension and shock syndrome. In: Wintrobe MM, Thorn GW, Adams R, Braunwald E, isselbacher K, Petersdorf R, eds.Principles of Internal Medicine (Seventh) New York: McGraw-Hill, 1974:185-186.

5. Walder LA, Schaller FA. Diagnostic cardiac catheterization. When is it appropriate? Postgrad Med 1995;97:37-42.

6. Skinner JS, Adams PC. Outpatient cardiac catheterisation. Int J Cardiol 1996;53:209-219.

7. Sondergaard L, Hildebrandt P, Lindvig Ket al. Valve area and cardiac output in aortic stenosis: quantification by magnetic resonance velocity mapping. Am Heart J 1993;126:1156-64.

8. Sondergaard L, Stahlberg F, Thomsen C, Stensgaard A, Lindvig K, Henriksen O. Accuracy and precision of MR velocity mapping in measurement of stenotic cross-sectional area, flow rate, and pressure gradient. J Magn Reson Imaging 1993;3:433-7.

9. Sondergaard L, Thomsen C, Stahlberg Fet al. Mitral and aortic valvular flow: quantification with MR phase mapping. J Magn Reson Imaging 1992;2:295-302.

10. Urchuk SN, Plewes DB. A velocity correlation method for measuring vascular compliance using MR imaging. J Magn Reson Imaging 1995;5:628-34.

11. Plewes DB, Urchuk SN, Kim S, Soutar I. An MR compatible flow simulator for intravascular pressure simulation. Med Phys 1995;22:1111-5.

12. Urchuk SN, Plewes DB. MR measurements of pulsatile pressure gradients. J Magn Reson Imaging 1994;4:829-36.

13. Tyszka JM, Laidlaw DH, Silverman JM. Relative pressure mapping using high-speed three-dimensional phase contrast cine MR imaging. Radiology 1997;205:304-304.

14. Pelc NJ, Herfkens RJ, Shimakawa A, Enzmann DR. Phase contrast cine magnetic resonance imaging. Magn Reson Q 1991;7:229-54.

15. Pelc NJ, Sommer FG, Li KC, Brosnan TJ, Herfkens RJ, Enzmann DR. Quantitative magnetic resonance flow imaging. Magn Reson Q 1994;10:125-47.

16. Wigstrom L, Sjoqvist L, Wranne B. Temporally resolved 3D phase-contrast imaging. Magn Reson Med 1996;36:800-3.

17. Pelc NJ, Bernstein MA, Shimakawa A, Glover GH. Encoding strategies for three-direction phase-contrast MR imaging of flow. J Magn Reson Imaging 1991;1:405-13.

18. Polzin J, Frayne R, Grist T, Mistretta C. Frequency response of multi-phase segmented k-space phase-contrast. Magnetic Resonance in Medicine 1996;35:755-762.

19. Szumowski J, Coshow WR, Li F, Quinn SF. Phase unwrapping in the three-point Dixon method for fat suppression MR imaging. Radiology 1994;192:555-561.

FIGURE CAPTIONS

Figure 1. Schematic diagram of the pulsatile flow generator and compliant phantom used to verify the numerical relative pressure calculation. Flow was generated by a centrifugal pump and modulated by a simple faucet driven by a DC motor. Two pressure transducers were mounted at each end of the rubber tube to monitor the entrance and exit pressure waveforms. Transducer signals and a gating trigger from the flow modulator were recorded on a laptop computer. Volume flow rates of approximately 25 ml/s were obtained at a pulsatile frequency of 68bpm.

Figure 2. Comparison of the longitudinal velocity component at the center of the tube (a-c) and volume flow rate (d-f) measured by 2D CINE PC (filled circles) and 4D PC (empty circles). Measurements were in slices passing through the stationary reference vials adjacent to the tube at the entrance (a and d), middle (b and e) and exit (c and f). The 2D slices were 5mm thick and the 3D slices extracted from the volume dataset were 1.9mm thick. All measurements account for the changes in cross-sectional area due to pulsatile flow. Note that the pulse amplitude decays with distance from the entrance, and that for both sequences, the pulsatile VFR tends to the mean VFR of −24.6 ml/s as measured by timed fluid collection (dotted line in (d-f)). The sign of the velocity was determined by the flow encoding gradient direction, which in this case was antiparallel to the flow.

Figure 3. Compliance as a function of relative pressure in the thin-walled rubber tube according to Eq.(3). Measurements were made at three locations (entrance, middle and exit) in the latex tube. The pressure scale has an arbitrary origin but covers the range of pressures encountered during the pulsatile flow experiment

Figure 4. Image data for the tube phantom. (a) Magnetization magnitude images of the central slice through the 4D PC dataset of the compliant tube phantom at each of the 19 temporal phases. (b) The velocity component parallel to the long axis of the tube. (c) The median filtered pressure gradient

calculated directly from the velocity information in (b) using the Navier-Stokes equation. (d) Relative pressure data calculated by integration and iterative refinement of the pressure gradient data in (c).

Figure 5. (a) Gage pressure waveforms from both the pressure transducers (thick and thin lines) over one period of the pulsatile waveform in the compliant phantom. The pressure waveforms are averages of approximately 60 cycles following Fourier interpolation to 128 points/cycle. (b) Comparison of the mean pressure difference across the rubber tube segment measured by the transducers (thick line) and the pressure difference calculated from the velocity images (thin line with circles indicating sample points). The effect of the frequency response of the 4D PC sequence can be seen as a temporal blurring and a reduction in amplitude of the waveform compared to the pressure transducer data. A slight phase shift between the two waveforms is also seen and is most probably a consequence of the gate detection method used by the MRI system. (c) The location of the origin (O) and measurement point (A) used to calculate the pressure difference waveform from the 4D PC data. These points correspond to the center of the tube closest to the pressure transducers.

Figure 6. *In vivo* relative pressure calculation using the same methods as for the pulsatile flow phantom. The magnetization magnitude (A) and superior-inferior velocity component (B) are shown at peak systole (19^{th} phase in the dataset). The superior-inferior component of the pressure gradient calculated from the velocity data is shown during (C) early systole (18^{th} phase) and (D) late systole (2^{nd} phase). The relative pressure maps corresponding to (C) and (D) are shown in (E) and (F) respectively. The aortic root is visible in these slices, but is not contiguous with the arch and descending aorta in the volume dataset. Consequently, the relative pressure map in the aortic root cannot be compared with that in the arch and descending aorta and is not included in subsequent processing. The images below have been cropped (the full field of view is shown in Figure 7). All sagittal images represent a 3mm thick slice through the center of the 3D volume data. A 1.9mm thick axial slice from the volume datasets at the level of the dashed line in (A) is shown immediately below each sagittal image. The grayscale ranges for the velocity, pressure gradient and pressure images are indicated at the bottom of the figure.

Figure 7. Relative pressure waveforms extracted from the relative pressure maps at points A (filled circles) and B (empty squares) in the aortic lumen. The pressure was referenced to point O in the distal descending aorta. All three points lie in the same 3mm slice of the 3D dataset. The pressure rises above zero at the start of systole during the accelerative phase (600ms to 700ms), then becomes negative during late systole during the decelerative phase (700ms to 1000ms). A transient increase in relative pressure is seen at 0.8s that may correspond to the arrival of a reflected wave from the distal aorta. Two periods of the pressure waveform are shown for clarity using the time scale corresponding to the peripheral gate.

TOP

Figure 1

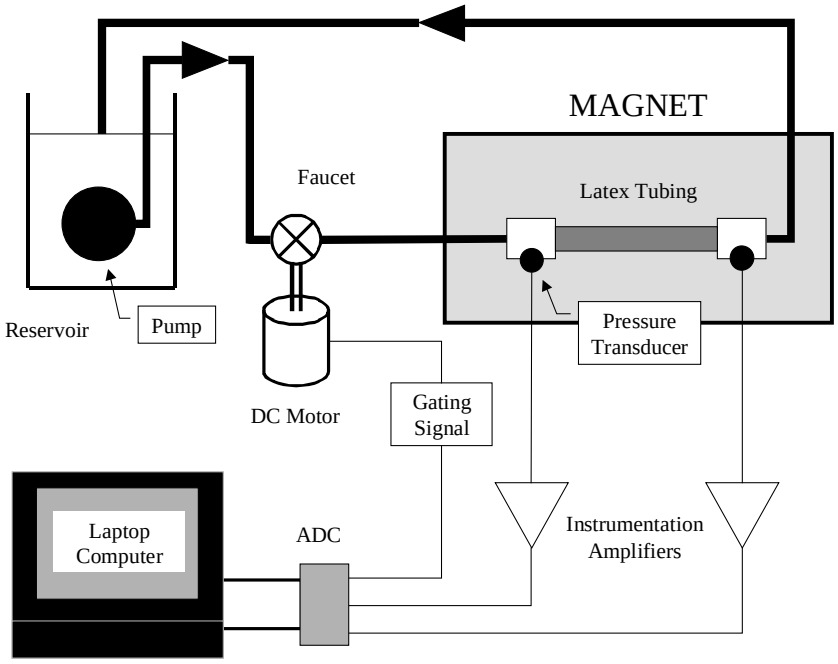
MAGNET
Faucet
Latex Tubing
Reservoir
Pump
Pressure Transducer
DC Motor
Gating Signal
Laptop Computer
ADC
Instrumentation Amplifiers

TOP

Figure 2

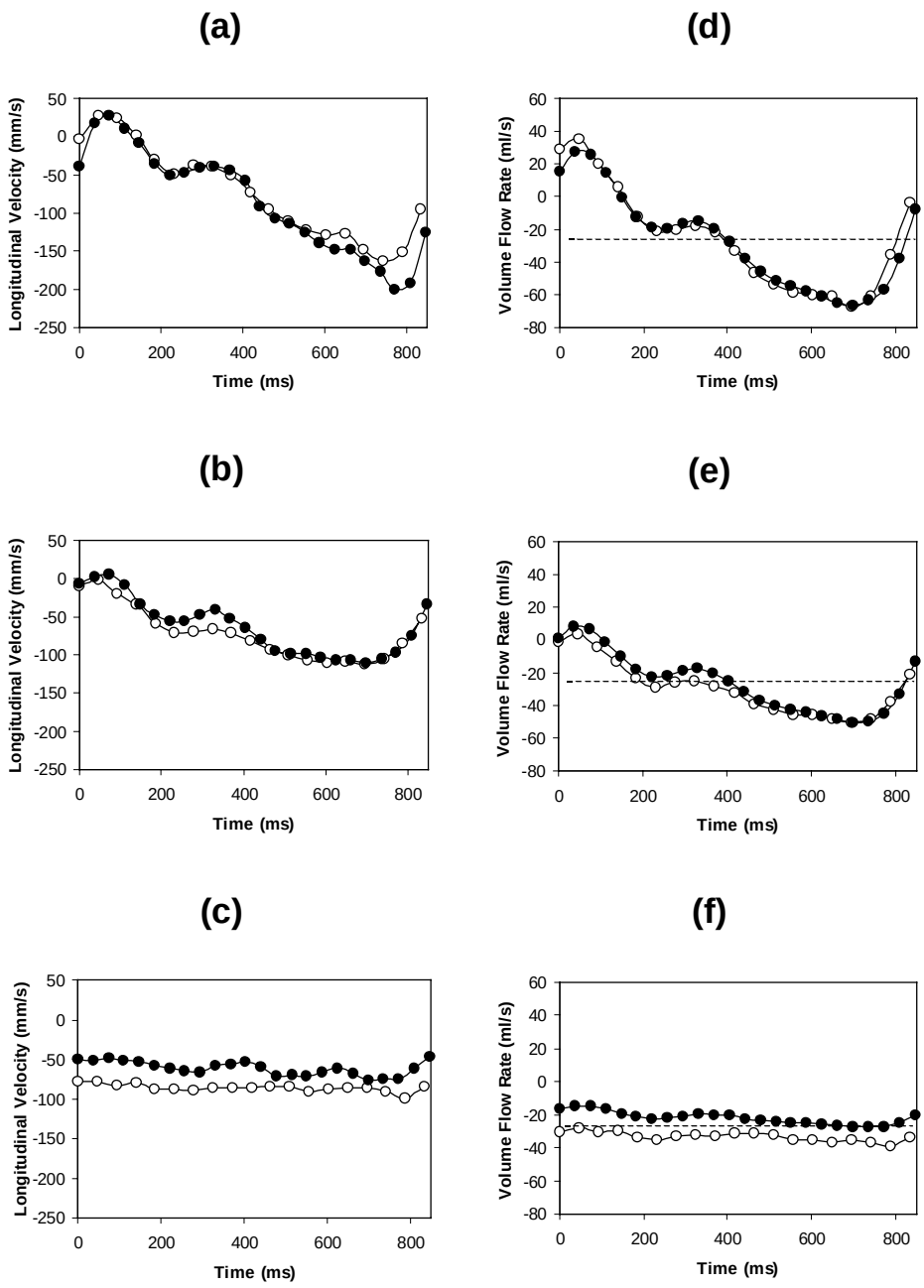
(a)
(d)
(b)
(e)
(c)
(f)
Longitudinal Velocity (mm/s)
Volume Flow Rate (ml/s)
Time (ms)
50
0
-50
-100
-150
-200
-250
60
40
20
-20
-40
-60
-80
0
200
400
600
800

TOP

Figure 3

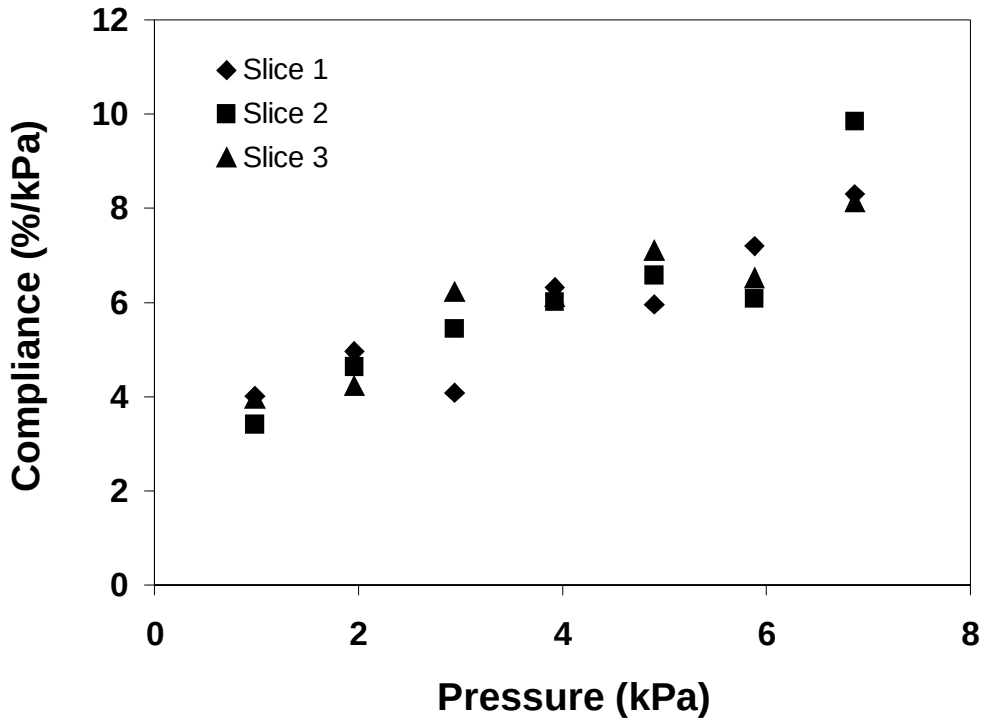
Slice 1
Slice 2
Slice 3
Compliance (%/kPa)
Pressure (kPa)
0
2
4
6
8
10
12
0
2
4
6
8

TOP

Figure 4

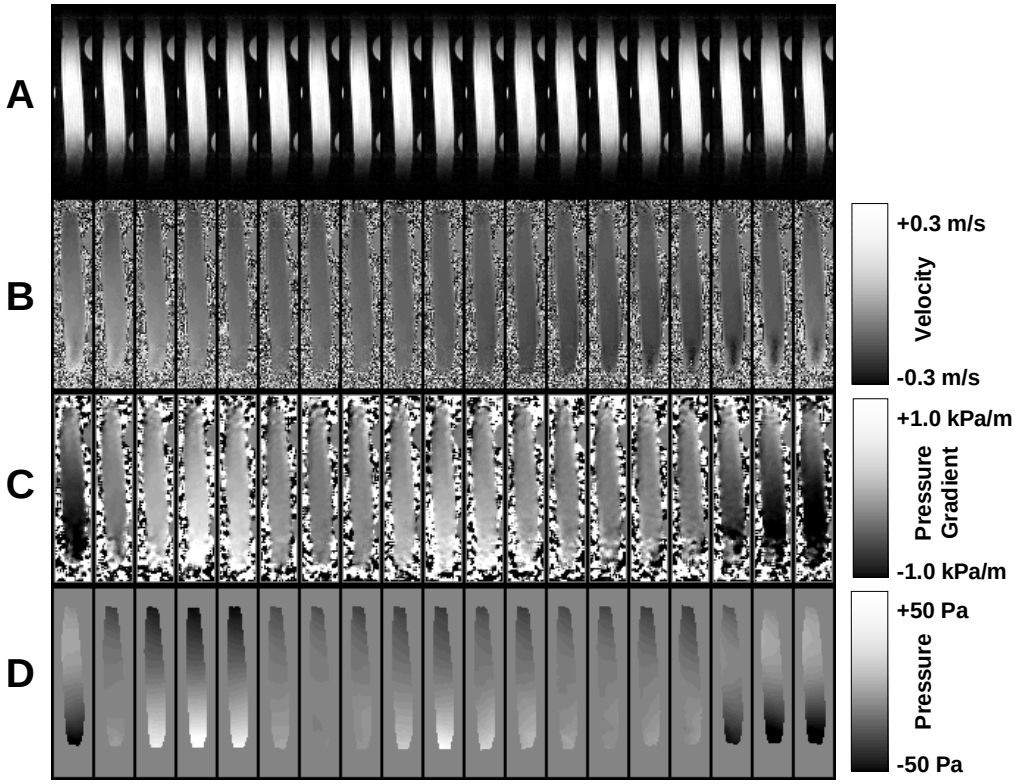
A
B
C
D
+0.3 m/s
Velocity
-0.3 m/s
+1.0 kPa/m
Pressure Gradient
-1.0 kPa/m
+50 Pa
Pressure
-50 Pa

TOP

Figure 5

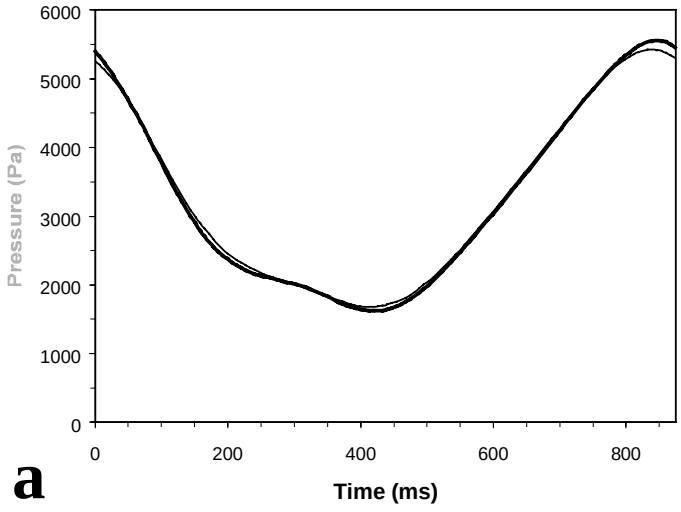

a

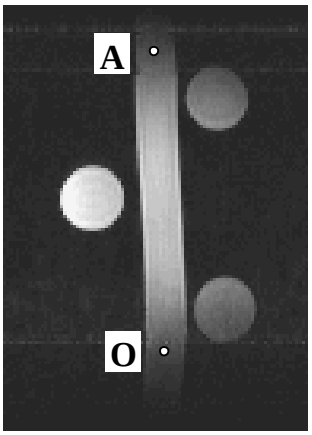

c

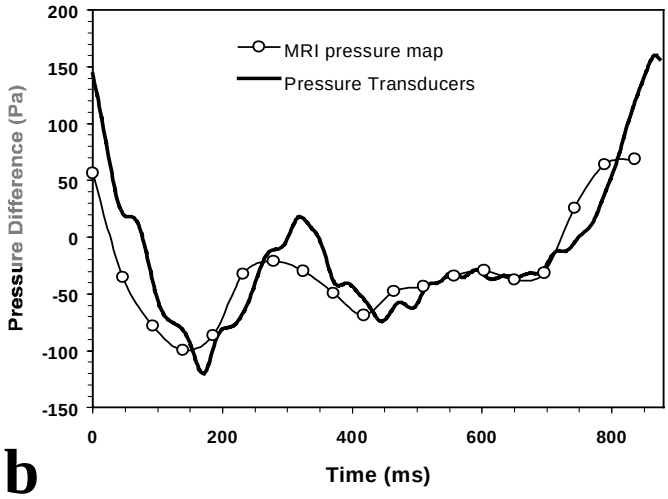

b

Figure 6

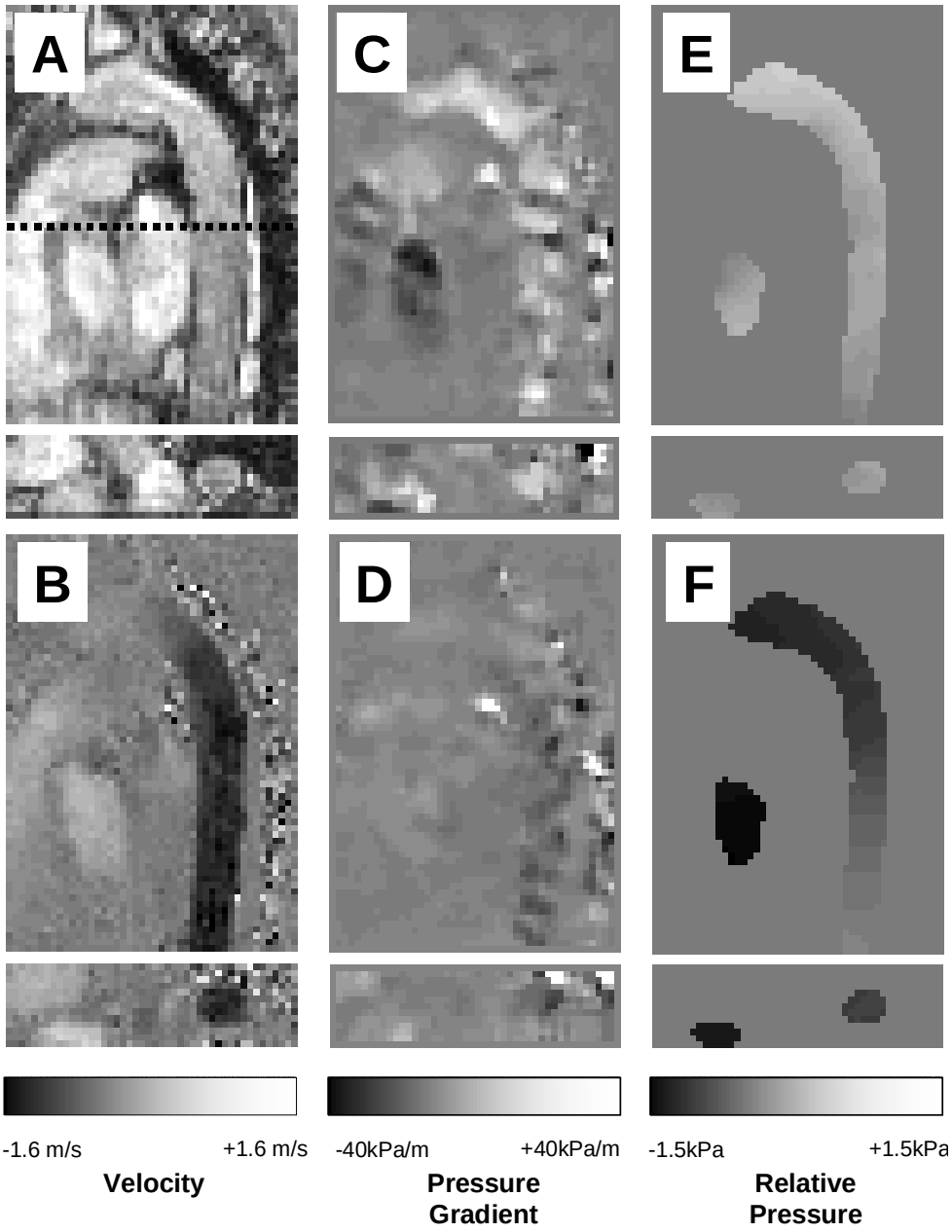
A
C
E
B
D
F
-1.6 m/s
+1.6 m/s
Velocity
-40kPa/m
+40kPa/m
Pressure Gradient
-1.5kPa
+1.5kPa
Relative Pressure

TOP

Figure 7

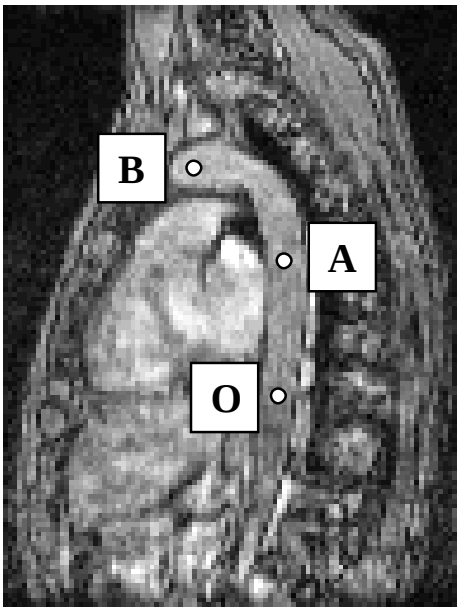
B
A
O

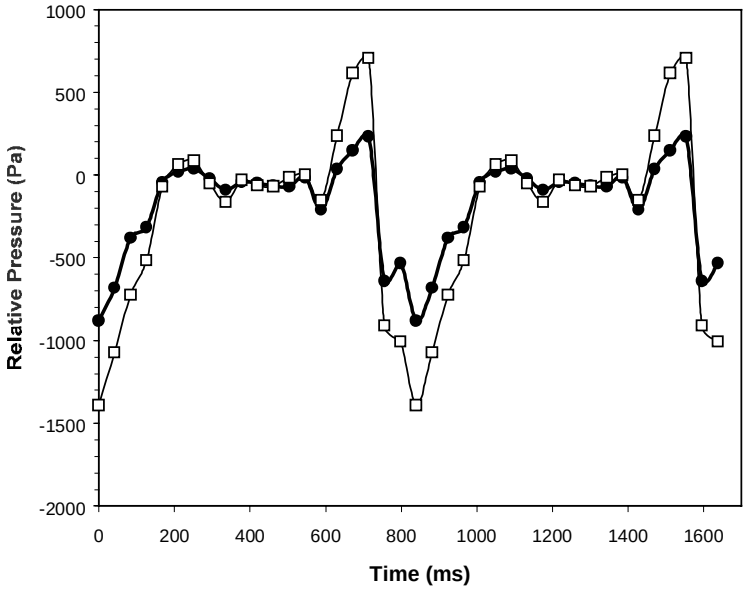
1000
500
0
-500
-1000
-1500
-2000
Relative Pressure (Pa)
0
200
400
600
800
1000
1200
1400
1600
Time (ms)